Proton imaging with machine learning

Finneman, G., Meskell, N., Caplice, T., Eichhorn, O., Abu-Halawa, A., et al.

G. M. Finneman, N. Meskell, T. Caplice, O. Eichhorn, A. Abu-Halawa, M. Stobb, U. Akgun, "Proton imaging with machine learning," Proc. SPIE 11595, Medical Imaging 2021: Physics of Medical Imaging, 1159551 (15 February 2021); doi: 10.1117/12.2580618

SPIE.

Event: SPIE Medical Imaging, 2021, Online Only

Proton Imaging with Machine Learning

G. M. Finneman, N. Meskell, T. Caplice, O. Eichhorn, A. Abu-Halawa, M. Stobb, U. Akgun
Coe College,
Cedar Rapids, IA, U.S.A.

Abstract:

The purpose of this study is to introduce a compact calorimeter that can offer an additional imaging tool for proton therapy centers. The tungsten, gadolinium, and lanthanide based high-density scintillating glass designed for this purpose has the ability to stop 200 MeV protons with thicknesses less than 60 mm, which allows us to model a compact detector that can be attached to a gantry. The details of the glass development and preliminary imaging efforts with this detector were previously reported.

This study summarizes the Artificial Neural Network based imaging efforts with this novel proton imager detector. A library of proton conical beam CT (CBCT) scans of 800 tumors was created via GATE simulations. This tumor library was used for training purposes with two different machine learning tools, Flux and PyTorch. Here, the proof-of-concept machine learning imaging study is reported. The novel material development, compact detector design, and machine learning based imaging can make this approach useful for clinical applications.

INTRODUCTION

Background

The idea of using protons in medical imaging for the purpose of proton therapy has long been known [1]. Although the proton radiography has seen some limited use in clinical applications such as range verification as well as quality control [2-8], proton tomography (pCT) has no current application in clinical use. However, increase in new proton therapy centers, and encouraging new developments in detector and data acquisition technologies makes pCT a near-future possibility [9-22].

The fundamental advantage of using protons (and ions) in radiation therapy is their capability to deliver a high dose of radiation to the tumor, compared to photon beams. Especially the Intensity Modulated Proton Therapy (IMPT), which uses pencil-beam to scan the patient, achieving a good control of the dose distribution and sparing the critical organs [23,24]. However, the "range problem" persists as the main difficulty to be resolved in proton therapy. The stopping power of the tissue determines the range of the therapy protons within the body, and current practice is to estimate them from using the x-ray CT images. The linear attenuation coefficients of x-rays are measured in Hounsfield units and converted to proton Relative Stopping Power (RSP). This conversion is calibrated by measuring the path of the protons within water and x-ray attenuation within different tissue materials. Nevertheless, the fundamental difference between proton and photon interaction within the materials produce the proton range uncertainties that can be as much as 5% in the abdomen, and up to 11% in the head, typically 1-3 mm [25-27].

Medical Imaging 2021: Physics of Medical Imaging, edited by Hilde Bosmans, Wei Zhao, Lifeng Yu, Proceedings of SPIE Vol. 11595, 1159551 · © 2021 SPIE
CCC code: 1605-7422/21/$21 · doi: 10.1117/12.2580618

If one calculates the proton RSP within the tissue directly with pCT, these range issues can be reduced. Another approach can be combined use of dual-energy CT with pCT to improve resolve the errors originating from Hounsfield unit to RSP conversions. The pCT development efforts motivated with this aim mostly focus on single-tracking systems, which track every proton within the pencil beam that scans the patient. In order to achieve the demanding task of tracking every proton, these pCT designs typically employ sophisticated tracker systems on both sides of the phantom, as well as a range detector that determines the Bragg peak location of the protons traversing the phantom [28-35].

All of these detector designs and the constructed prototypes use multiple layers of scintillating fiber or silicon strip trackers systems, and a calorimeter or a range detector for Bragg peak determination. The challenges of this approach can be summarized as the following:

i) The scintillating fiber-based tracker systems have low detection efficiency, even with the best silicon strip trackers the spatial resolution near the center of the phantom cannot be better than 0.5 mm.
ii) Tracking individual protons crates rate limitation on data acquisition systems, which either requires longer scan times or low image resolution.
iii) Multiple scattering of protons within the phantom is the main challenge of the image reconstruction. The proton path within the phantom is modelled as a straight line, cubic spline, or most likely path approximation [36].

The most promising reconstructed image was generated by LLU-UCSC Phase-II scanner showed that it is capable of achieving the best spatial resolution of about 2 mm [37,38]. Still, even the best reported prototype can complete a scan and image creation within ~15 minutes with considerable computational resources, and these designs are not suitable to be attached to a gantry [9].

A Compact Glass Detector for pCT

To handle the pCT problems listed above, the authors of this study proposed to use the proton bunches for pCT with a compact range detector design that can be attached to the gantry. The tungsten, gadolinium, and lanthanide based high-density scintillating glass developed for this calorimeter (named **CARNA** (**C**ompact gl**A**ss p**R**oto**N** im**A**ger) has the ability to stop 250 MeV protons with thicknesses less than 7 cm. The high novel density scintillating glass with the composition of 0.25 (Gd_2O_3) - 0.55 (WO_3) - 0.2 ($2B_2O_3$) (weight %) doped with 1% europium oxide (see Fig. 1-A), has 5.89 g/cm^3 density, with a transparency cutoff at 350 nm. The glass shows the characteristic Europium spectra, with emissions at 591 nm, 653 nm, 700 nm, and peak emission at 612 nm. The difference between the transparency cutoff and the peak emission wavelength yields plenty of room for possible degradation due to operational irradiation. The detailed description of the glass synthesis is described elsewhere [39]. The Geant4 [40,41] studies show that the high-density composition of the glass stops 200 MeV protons within less than 6 cm, as shown in Fig. 1-B. This calibration curve was generated by simulating protons energies varying from 40 MeV to 200 MeV. At each energy, the average Bragg peak location of 10^6 protons was determined; the average standard deviation was calculated to be 0.468 mm [42].

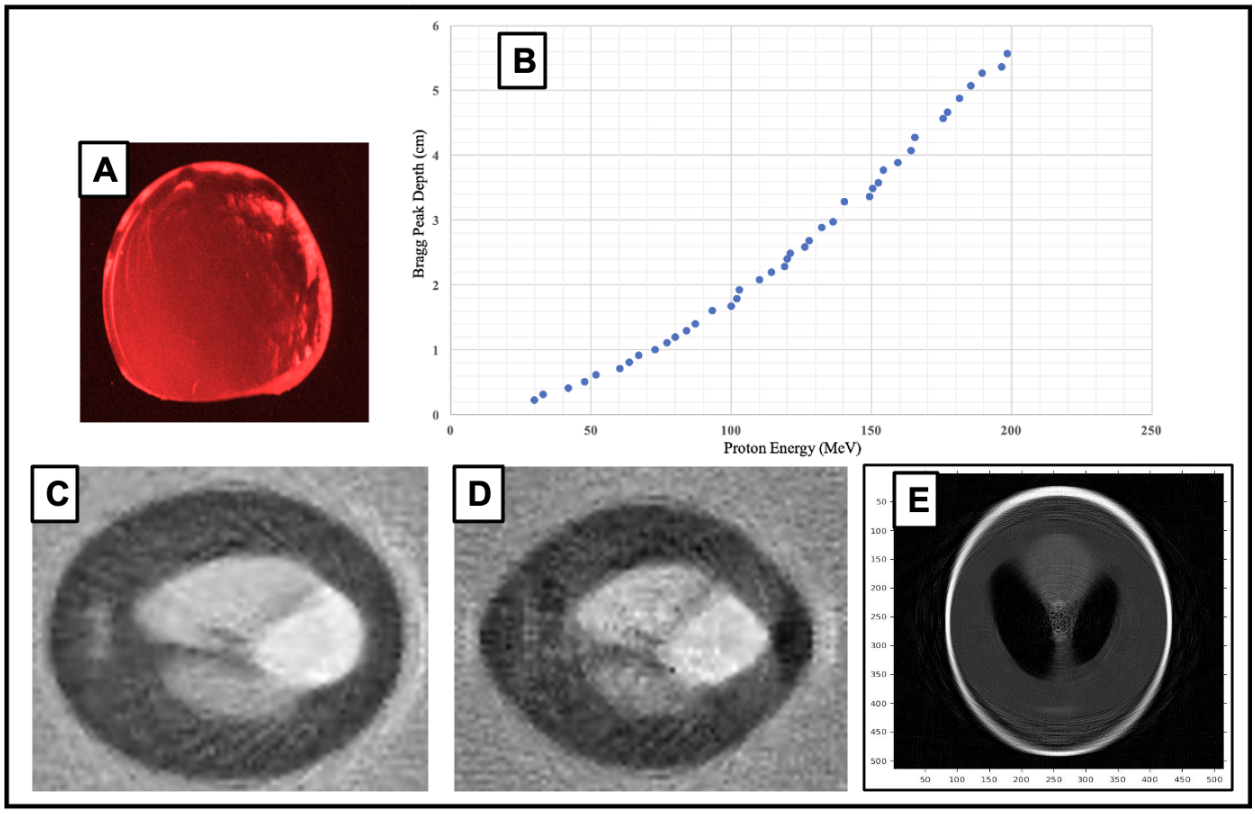

Figure 1: [A] The developed novel glass sample with UV excitation. **[B]** The Bragg peak position of proton beam within the 0.25 (Gd_2O_3) - 0.55 (WO_3) - 0.2 ($2B_2O_3$) doped with 1% europium oxide glass shows that less than 6 cm thickness is good enough to stop 200 MeV protons. **[C]** Reconstructed Shepp-Logan phantom images after Straight Line Path algorithm applied to the pencil beam. **[D]** Reconstructed Shepp-Logan phantom images after Cubic Spline Path algorithm applied to the pencil beam. **[E]** The reconstructed image of the Shepp-Logan phantom by using the neural network approach based on radon transformation.

The CARNA design is composed of 70 layers of 1 mm x 1 mm x 10 cm scintillating glass bars. Each layer, containing 100 such glass bars, oriented perpendicular to the adjacent layer. This alternating orientation of the adjacent layers aims tracking the proton bunches back to the phantom. The previous report suggests that unlike individual protons, the weighted center of energy for the proton bunch follows more or less a straight path. It has been shown that one can apply Straight Line Path and Cubic Spline Path and reconstruct the tumor image from simulated proton CTs with CARNA (see Fig. 1-C, and 1-D) [43]. The most recent study reported with CARNA calorimeter design shows that a proof-of-concept machine learning approach can be applied to improve the image quality (see Fig. 1-E) [44]. These reports combined with the others [45], show the viability of a successful image reconstruction via pencil beam either with machine learning or traditional reconstruction techniques.

Here, we report another machine learning approach which uses a scintillating glass based, 2-D, pixelated, "simpler" plane detector geometry (see Fig. 2). This report focuses on building a large neural network training dataset using the real tumor images from the Cancer Imaging Archive.

Currently, 800 tumors were selected, their pCT simulations were completed using pencil-beam with GATE [46-48]. We report the successful 3-D image reconstruction using two separate machine learning algorithms, based on Flux and PyTorch.

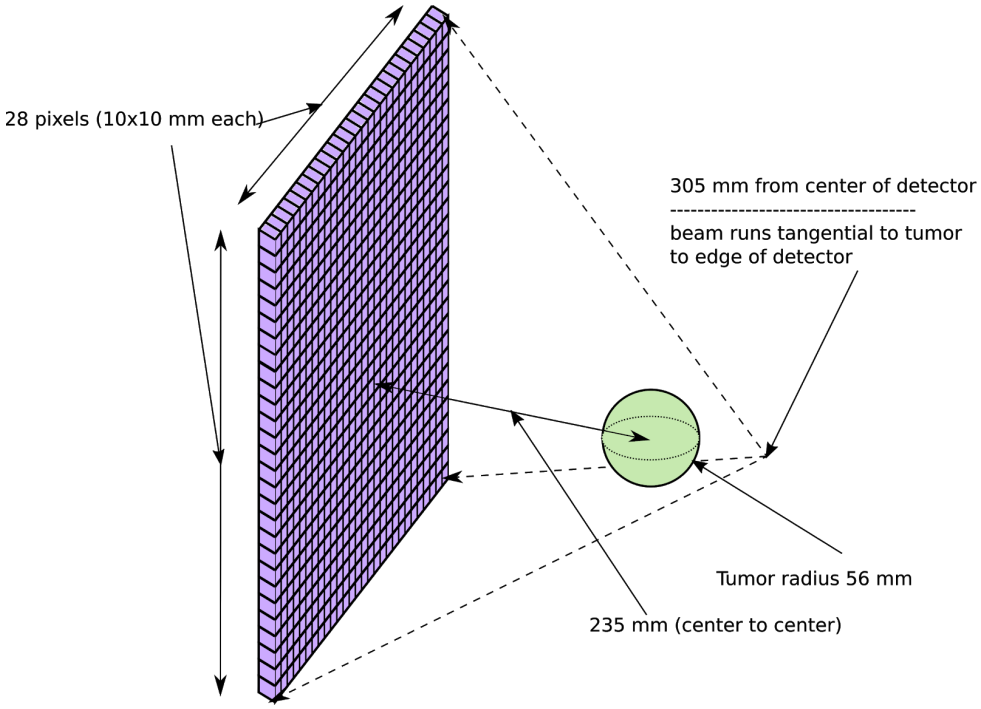

Figure 2: 28 cm x 28 cm flat panel detector model composed of 28 x 28 scintillating high density glass pixels.

METHODS

Tumor Selection and Processing

In order to create a training dataset that can represent a good set of physiologically relevant tumor shapes real tumor datasets were utilized. The training dataset for the machine learning process was selected from the Cancer Imaging Archive. Total of 800 tumors were collected from The Cancer Genome Atlas Cervical Kidney renal papillary cell carcinoma data collection (TCGA-KIRP) [49], invasive breast cancer dataset (Breast-MRI-NACT-Pilot) [50], Cervical Squamous Cell Carcinoma and Endocervical Adenocarcinoma data collection (TCGA-CESC) [51], FDG-PET/CT and radiotherapy planning CT imaging data (Head-Neck-PET-CT) [52], The Cancer Genome Atlas Head-Neck Squamous Cell Carcinoma data collection (TCGA-HNSC) [53]. Each tumor's DICOM files, which consists of a series of sliced images, were converted into a single MetaImage file by using NIH-ImageJ software [54].

The tumors which have enough size and saturation levels were resized to 28 x 28 x 28 voxels with each voxel having a side length of 2 mm. This ensured every tumor placed in the simulation was

centered, non-intersecting and spaced correctly from the detector and beam (see Fig. 3). Finally, these 5.6 cm x 5.6 cm x 5.6 cm tumor models were used for proton CT simulations. The CT scans were simulated using Gate V8.2, Geant4 V10.5, and ITK V5.1.

Every simulation required geometries, particle type, particle energy, materials, densities, and locations to be defined. The materials used in making the detector crystals and surrounding air were written to a material file and read in at the beginning of each simulation. Since we wanted particle interaction between the tumor and our proton beam related to the density of the tumor, we defined a set of materials found in human tissue including cancers and made a hu-material file. Each material was then mapped to a corresponding voxel in the tumor image based on HU (Hounsfield units) values. The same was done for the densities of the voxels.

Each Tumor was different from the last in terms of Hu values, instead of dynamically writing a file for each tumor at the beginning of each simulation, we created an individual material and density file pair for every tumor. Every material file started out the same but their Hu numbers were altered to match the tumor they corresponded with. The simulation was then directed to use a tumor and its corresponding material and density files at the start of each simulation. Due to the large number of simulations, the regular changes and number of files being juggled, a script was created to iterate through the available tumors and corresponding files automatically and alter the paths in the Gate macro file.

During the CT scan simulation, 10^7 protons with energies varying between 145 MeV to 150 MeV were shot at each 6 degrees rotation of the phantom. By this way 60 datasets were generated for each tumor's CT scan.

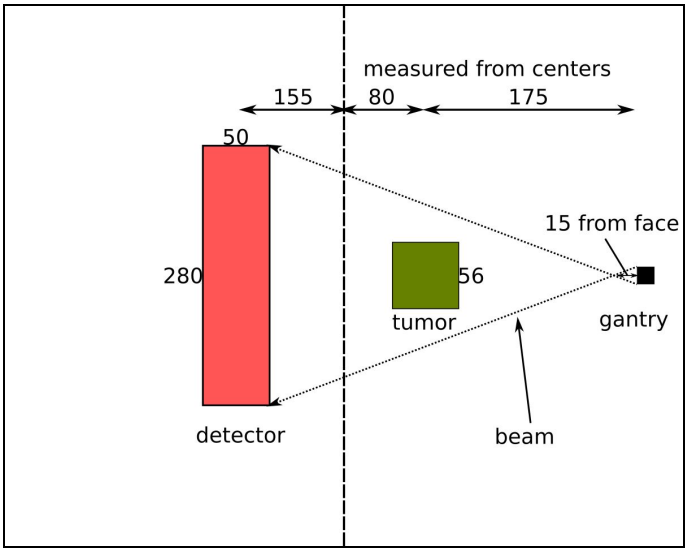

Figure 3: The dimensions of the GATE simulation model. This is a top view showing the pencil beam covering the whole tumor.

Neural Network Development

The crucial point for this study was to come up with the efficient Neural Network (NN) that can predict 28 x 28 x 28 pixels tumor slices with 60 input images (28 x 28 each). Since the computational power to perform CBCT simulations are finite, the efficient NN was the main goal. While the 800 tumor CT scans were completed, the initial NN construction efforts started with the Fashion MNIST (FMNIST) dataset. FMNIST provides 28x28 pictures, same as the energy deposition that CT scans provide on the 28x28 pixelated detector. The FMNIST dataset is traditionally used as a Classification Neural Network training tool using Dense algorithms. Since the goal of the NN would be to have input tumor density image scans and output tumor images, for each FMNIST input image a target output image was created. This was done by reflecting the FMNIST along both axis' and inverting the values of each pixel. This Input-Target Output pair serves as the detector signal - 2D tumor projection of the CBCT simulations. 10,000 FMNIST pictures were selected as the initial training data to build a NN, that will yield good results with the minimum possible training set. Since this can be described as a classification problem, the initial unsuccessful attempts were using dense algorithms in Julia based Flux and Python based PyTorch tools. Later as the NN modified to use 2D Convolutional Neural Network, even with 250 training images the predictions of the AI started to succeed.

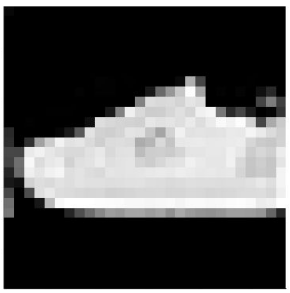

Input

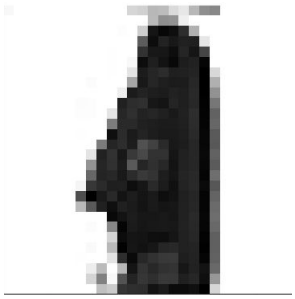

target output

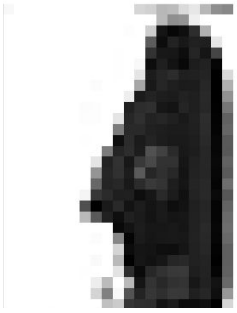

Target (dense)

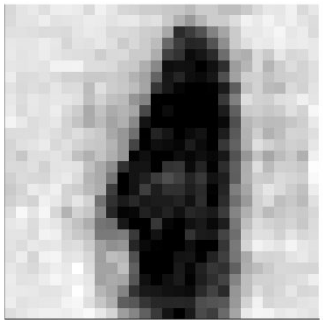

Flux output (dense)

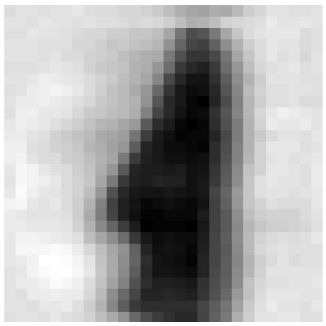

PyTorch output (dense)

Figure 4: [TOP-LEFT] Example 28x28 FMNIST image used for input, [RIGHT] target output generated for training purposes. [BOTTOM] The 2D CNN predictions of Flux and PyTorch after 250 image training with the FMNIST dataset.

As the 2D CNN was shown to be effective for this study, the same algorithms were used for the training dataset generated by the 800 tumor CBCT data generated in GATE. Some adjustments needed to be made, as the tumor input had not a single image, but 60 different images, each a different angle of the tumor density created in the GATE Simulation. Additionally, the output was not a 28x28 pixel image, but a 28x28x28 voxel density map. In order to overcome these issues, a 2D Convolutional Neural Network (CNN) with 60 input channels was used in both PyTorch and Flux. This allowed CNN to take in all 60 input images at once. The FMNIST NN output is a 1D array with 784 values, which we reshaped into a 28x28 pixel image. In order to change this into a 28x28x28 voxel image output, the output was changed into a 1D array with 21,952 values. This could be reshaped into the 28x28x28 voxel image, which would be trained to match the Cancer Imaging Archive tumors simulated through GATE. The optimizations yield slight differences on the design of the final deep learning algorithms used with Flux and PyTorch (see Figures 5 and 6).

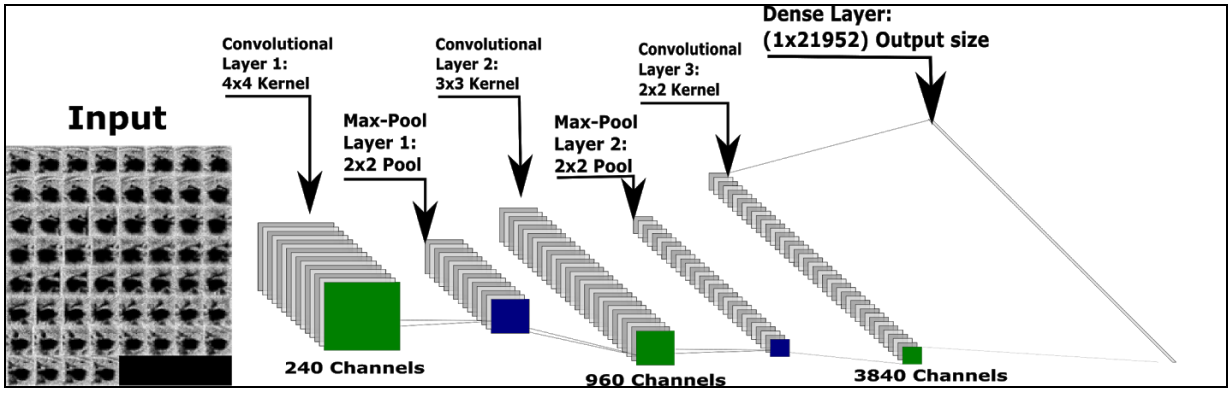

Figure 5: PyTorch NN architecture - Three 2D convolution layers with two max pooling layers followed by a single dense layer to adjust size of output. The image on the left shows 60 pictures, each with 28x28) showing the detector energy depositions obtained during the pencil beam CBCT scan simulations.

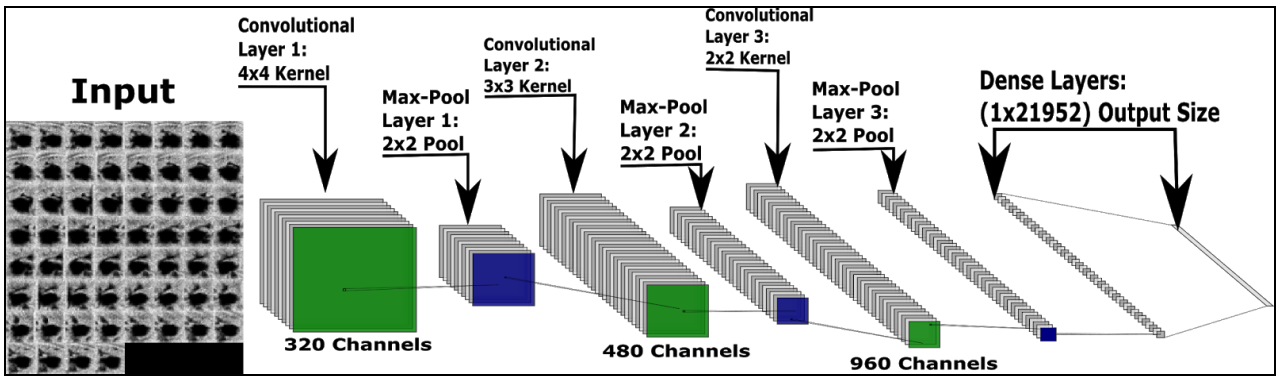

Figure 6: Flux NN architecture - Three 2D Convolutional Layers and three max pooling layers followed by two dense layers to adjust size of output. The image on the left shows 60 pictures, each with 28x28) showing the detector energy depositions obtained during the pencil beam CBCT scan simulations.

RESULTS

The tumor training and test data used by the NN have a high degree of similarity, due to the nature of the physical system. An early stopping procedure was used for the NN creation to prevent simple memorization and over training. This method stops training and saves the model whenever the validation loss stopped improving after a set patience. For PyTorch based NN, this patience was set at 10 epochs, or runs. Training would often stop after 100 epochs. The specifications for training included a batch size of 4. The optimizer was Adam and the loss function used was mean squared error. RELU was used as the activation function with a learning rate of .001. A 2 x 2 pooling layer was always used in conjunction with the 2d convolutional layers. Training was run on a GPU server in our lab for speed. PyTorch predicted some large features with the initially small training dataset (~120 tumors) but was beset by what appeared to be spots where a max density was filled in in the original predictions. It was unclear what was the cause of these spots, however, as the dataset grew the number of spots diminished (see Figure 7 - LEFT).

Originally, Flux based NN was trained with a triple-layered 3D Convolutional Neural Network (CNN) with one channel. For this approach, the different rotations of the tumor are used as the depth dimension. Ultimately it was decided that this would not be sufficient as it was likely that CNN would attempt to recognize features that exist across rotations when such features do not, in actuality, exist. This led to the final design, a 2D CNN that would examine each rotation as its own channel, thus with its own features that could be found.

The 2D CNN algorithm uses the 60 image angles input as different channels. This method was much more successful than the 3D CNN, and it was found that only 30 of the 60 image angles were needed. Also, the 3D CNN training time was found to be around four times longer than the 2D CNN algorithms. The 2D CNN Flux based NN algorithm given in Figure 6 trains 800 tumor dataset within

~30 min with a modest computer with 10 CPUs. This training time is comparable with the PyTorch NN training time although the later used a single GPU for this purpose. The Figure 7 right two columns show some sample 2D CT predictions by the Flux NN based on 2D CNN, along with the target slices from the test tumors.

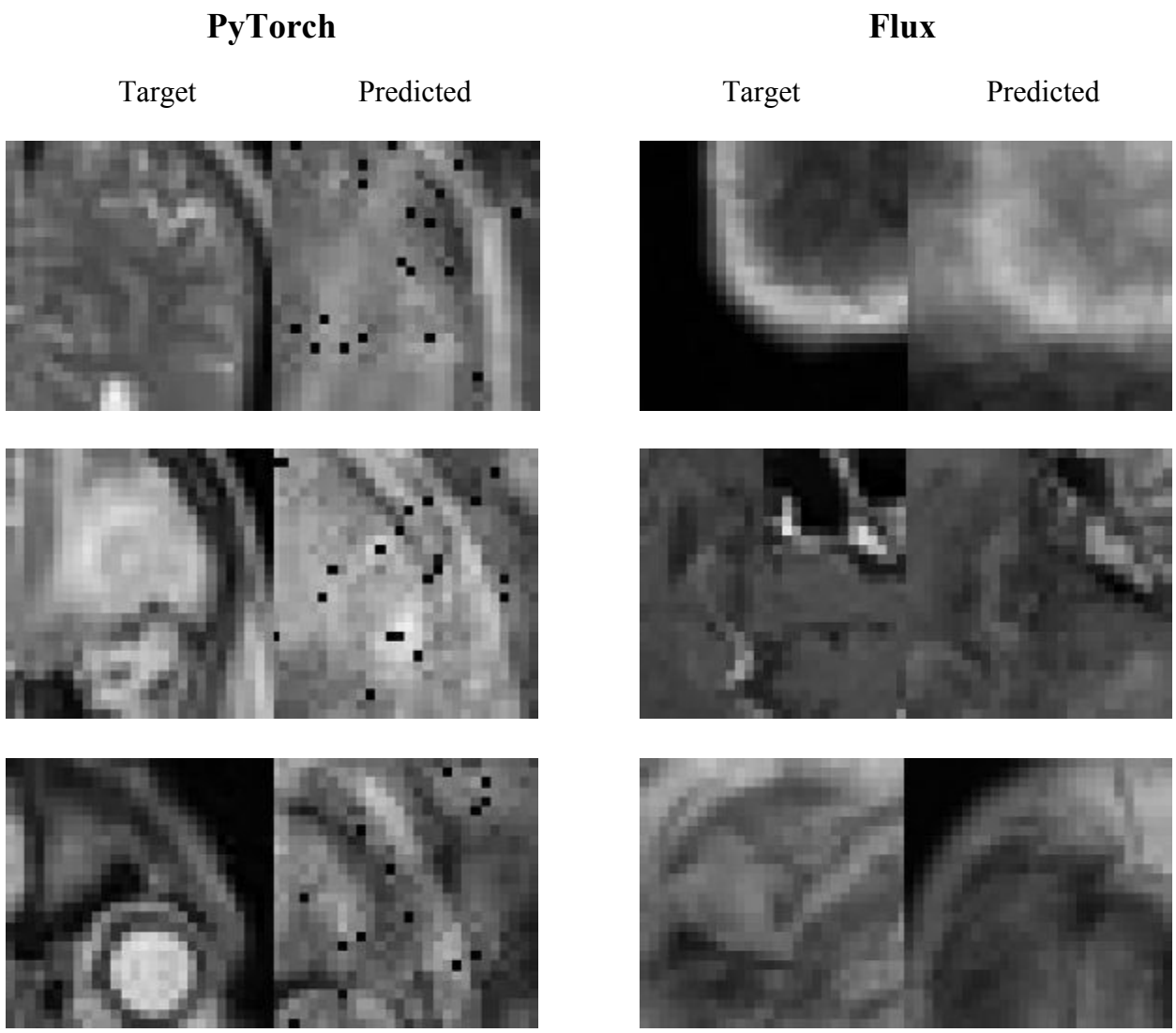

Figure 7: [LEFT] PyTorch trained NN reconstruction results - 2D image slices of 3 different tumors. In each image pair, original tumor on left and AI reconstruction on right. [RIGHT] Julia trained NN reconstruction results - 2D image slices of 3 different tumors. In each image pair, original tumor on left and trained NN reconstruction on right.

The neural network has been updated as the CBCT dataset continues to grow. By this way the effect of different datasets on the final prediction of the NN could be monitored. The first CBCT simulations were performed on brain tumors, since the skull creates a strong density contrast, it was a good training feature for the NNs. When around 250 tumor CBCT simulations were completed on entirely brain tumors, although the NN was not memorizing the data, it seemed to recognized the patterns with successful predictions. Figures 8 and 9 show the target as well as the 250 tumors and 800 tumors trained NN predictions for all 28 slices of the same brain tumor. This specific tumor was selected for this comparison since the skull represents a clear reference point to compare the predictions. These figures also clearly show that as the other tumor datasets were included to the training dataset, the NN predictions start to give less accurate outputs.

Finally, the Flux NN showed that there is a tradeoff between recognizing the patterns and predicting the tumor density. As one adds more layers, to increase the number of Max Pooling Layers, each layer compresses the data which in turn freeing memory for more channels. This, damages the structure of the input tumor, but the extra memory allows for more patterns to be learned. This results in better detail, but poorer overall tumor density understanding. Figure 10 shows such comparison between 7-layered CNN algorithm versus the 3-layered CNN algorithm. Although the 7-layered algorithm recognizes the patterns better; the 3-layered algorithm predicts the densities better.

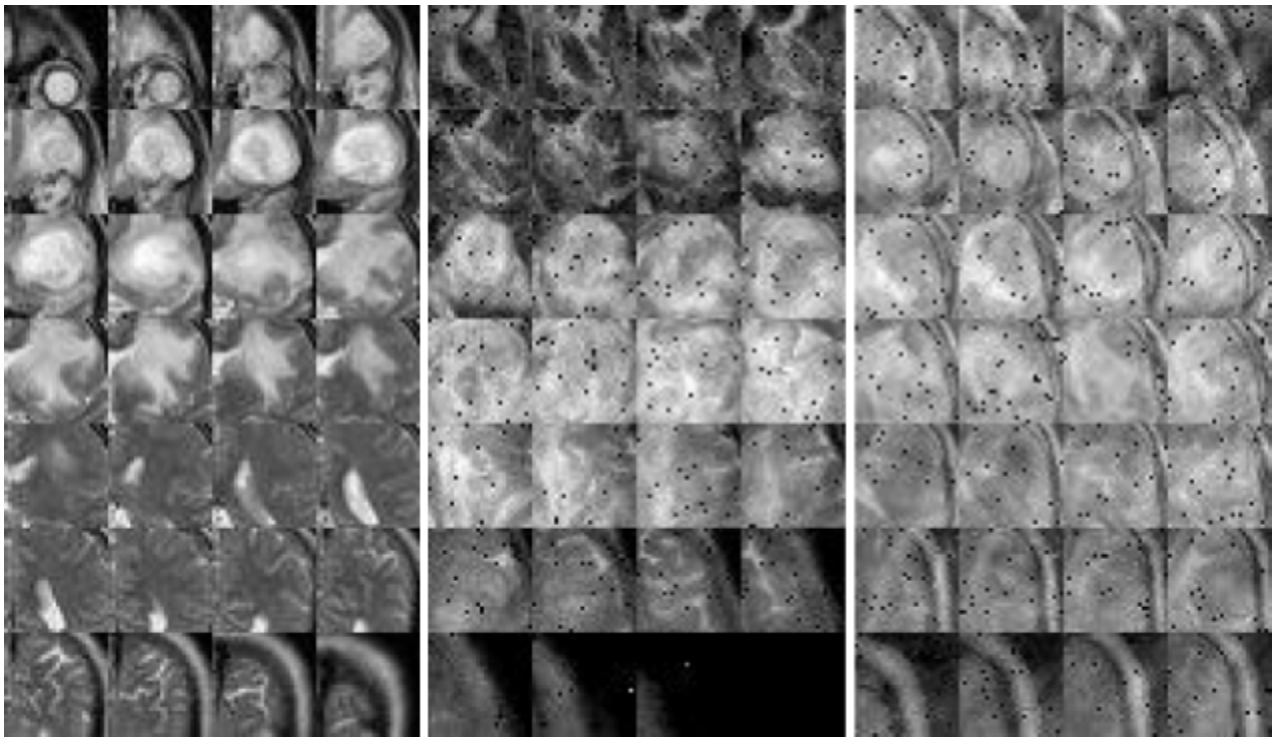

Target Output (250) Output (800)

Figure 8: A brain tumor prediction by PyTorch based NN. With 250 brain tumor training set,

prediction looks more successful compared to 800 tumor mixed training set.

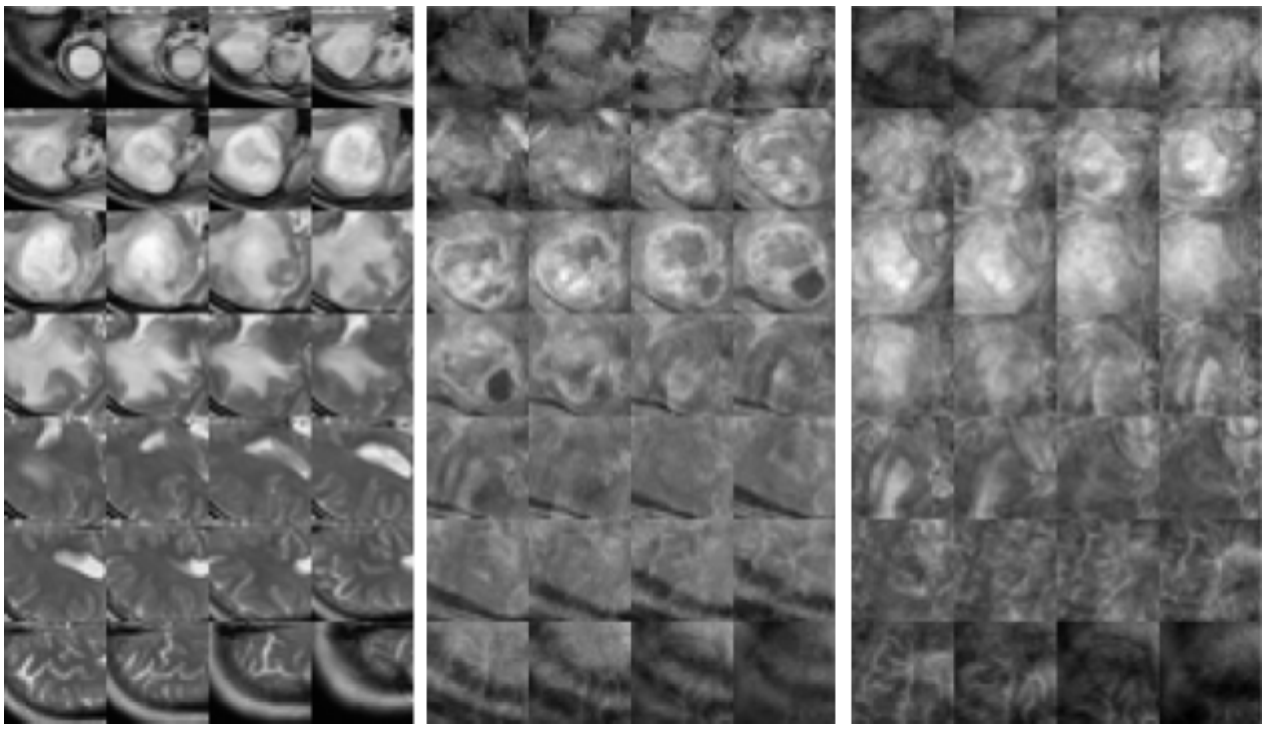

Target Output (250 tumor) Output (800 tumors)

Figure 9: A brain tumor prediction by Julia based NN. With 250 brain tumor training set, prediction looks more successful compared to 800 tumor mixed training set.

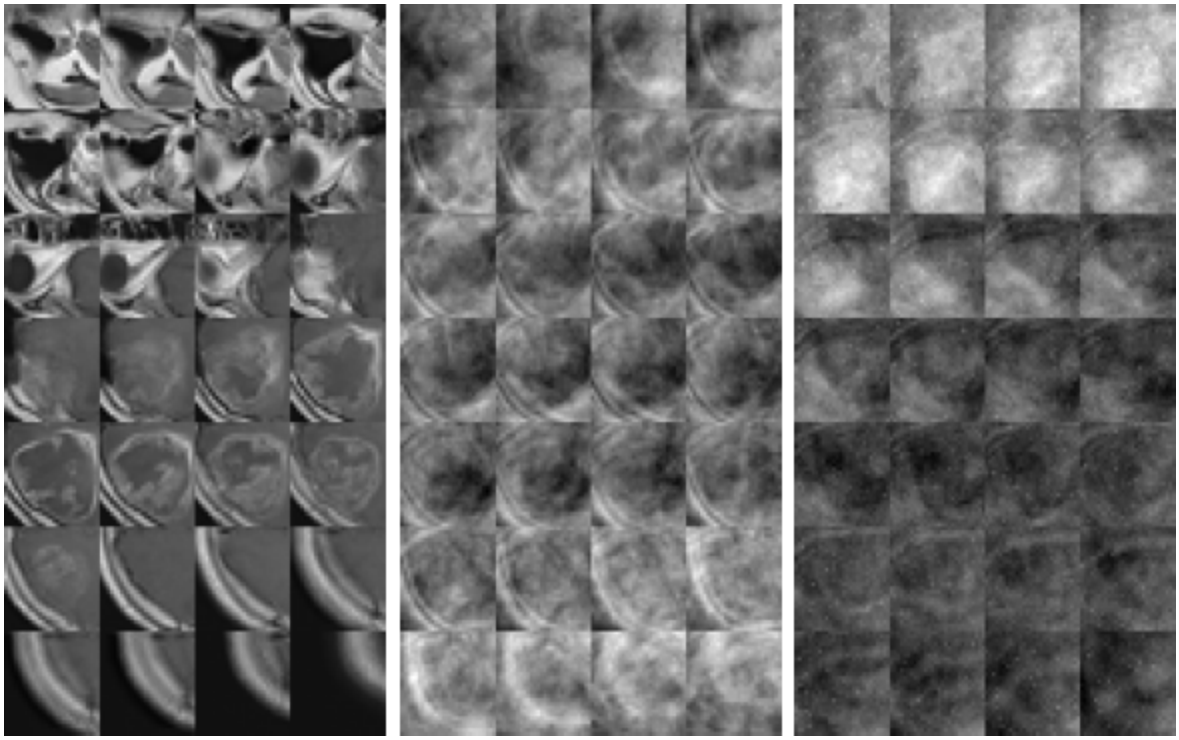

Figure 10: Mosaics of 3D density structures sliced into twenty-eight 2D slices. Light pixels represent higher densities. [LEFT] Target brain tumor, [MIDDLE] Seven layered algorithms reconstruction of the brain tumor. [RIGHT] Three layered algorithms reconstruction of the brain tumor.

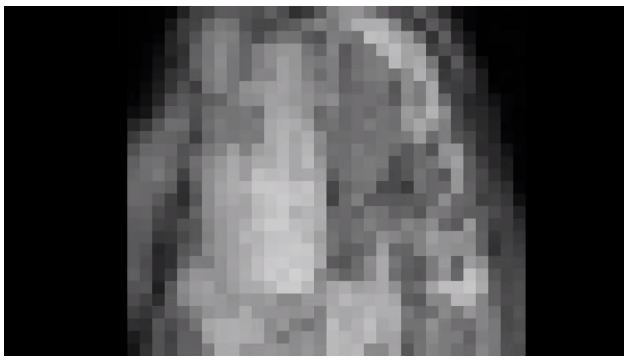

julia3DTarget1
First 3D target from Julia
http://dx.doi.org/10.1117/12.2580618.1

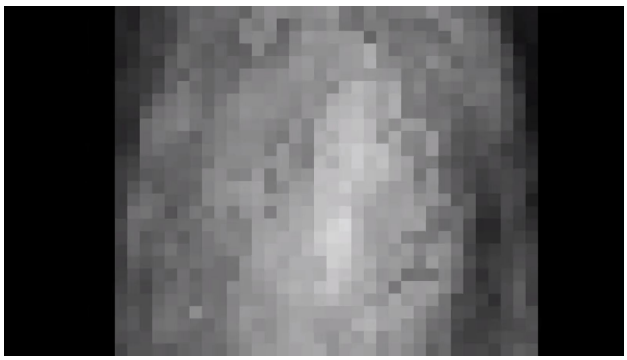

julia3DPrediction1
Prediction
http://dx.doi.org/10.1117/12.2580618.2

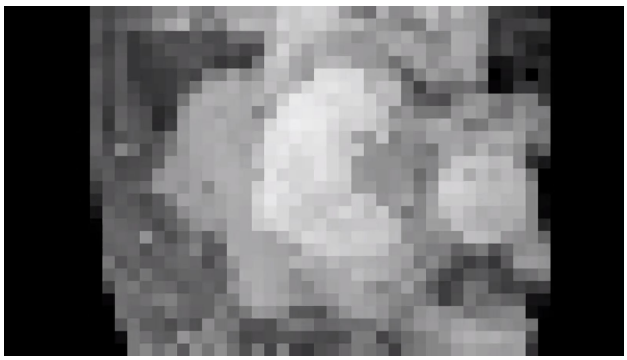

julia3DTarget2
Second 3D target from julia
http://dx.doi.org/10.1117/12.2580618.3

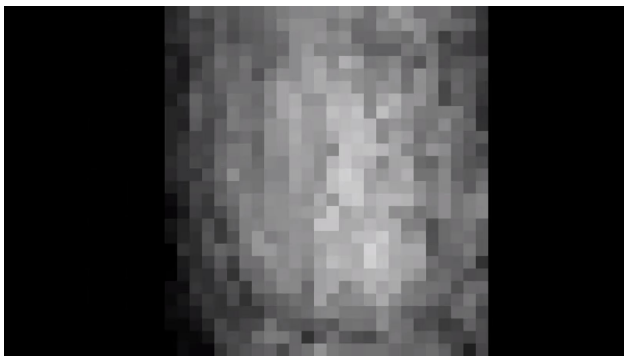

julia3DPrediction2
Prediction
http://dx.doi.org/10.1117/12.2580618.4

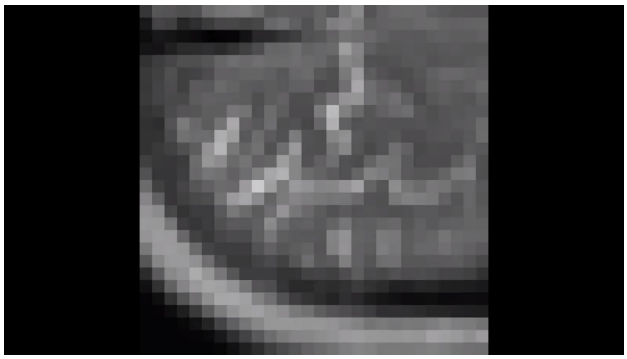

juliaSliceAnimationTarget
Scroll through target julia
http://
dx.doi.org/10.1117/12.2580618.5

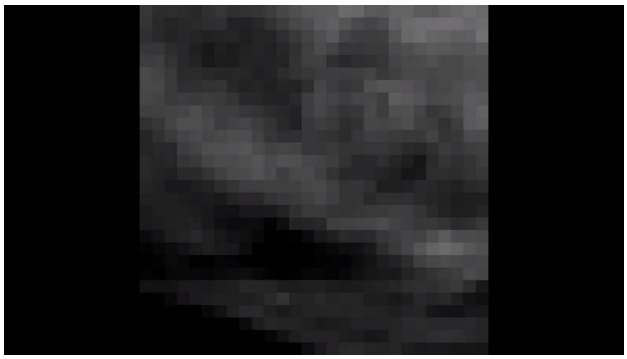

juliaSliceAnimationPrediction
Scroll through predicted julia
http://
dx.doi.org/10.1117/12.2580618.6

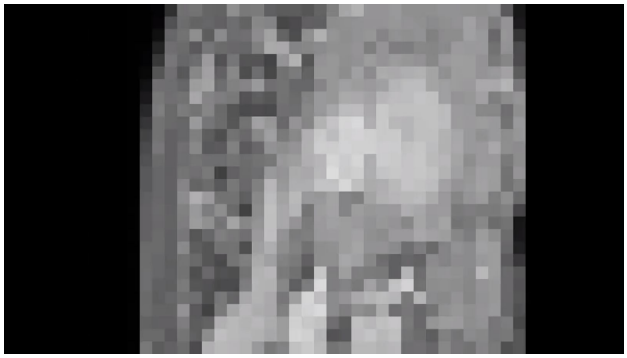

pytorch_target_rotation
Pytorch 3D target 1
http://dx.doi.org/10.1117/12.2580618.7

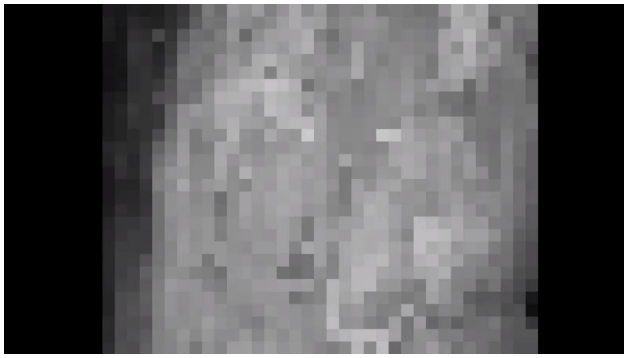

pytorch_pred_rotation
Prediction
http://dx.doi.org/10.1117/12.2580618.8

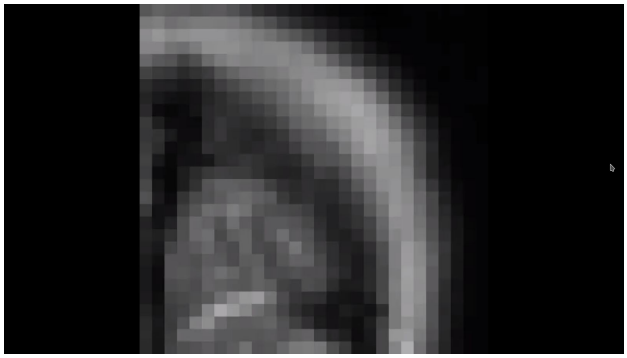

pytorch_target_scroll
Pytorch target scroll through
http://dx.doi.org/10.1117/12.2580618.9

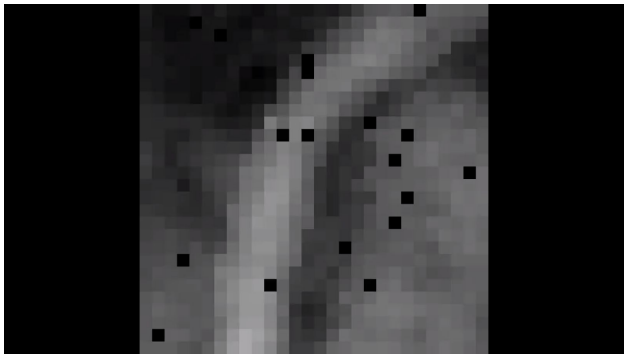

pytorch_pred_scroll
Pytorch prediction scroll through
http://dx.doi.org/10.1117/12.2580618.10

CONCLUSION & DISCUSSION

The hadron therapy provides a great advantage of depositing high dose radiation to the tumor while not damaging the healthy tissues less compared to the other radiation therapy beams. The range problem of the protons can be reduced by measuring (or calculating) the Relative Stopping Power within the tissue. This is the main aim behind the efforts for building pCT systems. The authors of this study had developed a novel high density scintillating glass that can be used for a compact calorimeter system that can stop 200 MeV protons within less than 6 cm.

This report summarizes the latest study that shows the feasibility of a compact, glass, imaging detector, that can be attached to gantry. Two different machine learning algorithms were developed, based on PyTorch and Flux, and tested with 800 tumors' simulated pCT. The tumors were selected from various datasets of the Cancer Imaging Archive, and their 3D structures were successfully predicted by both algorithms. The machine learning approach used in this report was implemented using two separate machine learning ecosystems. This allowed us to compare both their relative ease of use and performance using identical training and test data. While both implementations were able to produce reasonable tumor reproductions, the results from Flux appeared to be of higher quality. Additionally, the creation of the NN was syntactically simpler using Pytorch. This proof-of-concept study has promising findings, and lots of room for improvement;

i) The machine learning approach provides opportunity to reconstruct the images with less than 1000 tumor pCT used as the training set. The preliminary results reported here hints that the prediction can be better if the NN is trained with specific tumor dataset. i.e. instead of universal NN the future studies should test the effectiveness of specialized NNs for different tumor types.

ii) This study shows that the total radiation dose delivered to the phantom can be reduced even more compared to the X-ray CT. The simulated CT scans used 6 degrees step size, with 10^5 protons at each angle. This bare minimum simulation yields a radiation dose deposition of 0.04 mGy on the phantoms, which is dramatically less than the 1.3-1.4 mGy range reported on single proton pCT systems [22].
The next version of this study needs to increase the number of protons to 10^6-10^7, which is expected to improve the prediction quality, as well as the deposited radiation dose on the phantom. Here the CT scan step size is the crucial variable that needs to be optimized. The machine learning approach seems capable of yielding good predictions with coarser CT step sizes such as 10 degrees.

iii) The current detector design is 28 x 28 pixels, with 10 mm x 10 mm pixel cross section. These detector dimensions were chosen to make sure that the incoming pencil beam is completely captured by the detector. This compact design can easily be attached to the gantry, and does not require any tracker system, and once the NN is trained the prediction takes milliseconds in a single CPU computer.

The future study will focus some tumors smaller than 5.6 cm x 5.6 cm x 5.6 cm size, getting ready for a small animal test.

Now the future of this study should focus on how to implement this information to hadron therapy. One idea is to use this gantry-attached compact detector to improve dual energy x-ray CT images and see if we can reduce the error. Another approach might be to use this system as a standalone pCT device, which would be a more challenging task.

Acknowledgements

This work was supported by NSF-DMR 1746230, NSF-REU 1950337, McElroy Trust, and Coe College.

References

[1] Cormack A 1963 Representation of a function by its line integrals, with some radiological applications *J. Appl. Phys.* 34 2722
[2] Schneider U and Pedroni E 1995 Proton radiography as a tool for quality control in proton therapy *Med. Phys.* 22 353–63
[3] Steward V and Koehler A 1973 Proton radiographic detection of strokes *Nature* 245 38–40
[4] Steward V and Koehler A 1973 Proton beam radiography and tumor detection *Science* 179 913–4
[5] Steward V and Koehler A 1974 Proton radiography in the diagnosis of breast carcinoma *Radiology* 110 217–21
[6] Steward V and Koehler A 1974 Proton radiography of a human brain tumor within the skull: a preliminary report *Surg. Neurol.* 2 283–4
[7] Morris C, Hopson J and Goldstone P 2006 Proton radiography *Los Alamos Sci.* 30 32–45
[8] Parodi K 2014 Heavy ion radiography and tomography *Phys. Med.* 30 539–43
[9] Poludniowski G, Allinson N and Evans P 2015 Proton radiography and tomography with application to proton therapy *Br. J. Radiol.* 88 20150134
[10] Bashkirov V A *et al* 2016 Novel scintillation detector design and performance for proton radiography and computed tomography *Med. Phys.* 43 664
[11] Seco J and Depauw N 2011 Proof of principle study of the use of a cmos active pixel sensor for proton radiography *Med. Phys.* 38 622–3
[12] Poludniowski G *et al* 2014 Proton-couting radiography for proton therapy: a proof of principle using CMOS APS technology *Phys. Med. Biol.* 59 2569–81
[13] Braccini S *et al* 2010 First results on proton radiography with nuclear emulsion detectors *J. Instrum.* 5 P09001
[14] Testa M *et al* 2013 Proton radiography and proton computed tomography based on

time-resolved dose measurements *Phys. Med. Biol.* 58 8215–33
[15] Rinaldi I, Brons S, Gordon J, Panse R, Jäkel O and Parodi K 2013 Experimental characterization of a prototype detector system for carbon ion radiography and tomography *Phys. Med. Biol.* 58 413–27
[16] Doolan P, Testa M, Sharp G, Bentefour E, Royle G and Lu H-M 2015 Patient-specific stopping power calibration for proton therapy planning based on single-detector proton radiography *Phys. Med. Biol.* 60 1901–17
[17] Pemler P, Besserer J, de Boer J, Dellert M, Gahn C, Moosburger M, Schneider U, Pedroni F and Stäuble H 1999 A detector system for proton radiography on the gantry of the paul-scherrer-institute *Nucl. Instrum. Methods Phys. Res.* A 432 483–95
[18] Collins-Fekete C, Brousmiche S, Portillo S and Seco J 2016 A maximum likelihood method for high resolution proton radiography/proton CT *Phys. Med. Biol.* 61 8232–48
[19] Lo Presti D *et al* 2014 Optical fiber folded scintillating extended tracker *Nucl. Instrum. Methods* A 737 195–202 [88] Lo Presti D *et al* 2016 Design and characterization of a real time proton and carbon ion radiography system based on scintillating optical fibres *Phys. Med.* 32 1124–34
[20] Bucciantonio M, Amaldi U, Sauli F and Watts D 2013 Development of a fast proton range radiography system for quality assurance in hadrontherapy *Nucl. Instrum. Methods* A 732 564–7
[21] Amaldi U *et al* 2011 Construction, test and operation of a proton range radiography system *Nucl. Instrum. Methods* A 629 337–44
[22] Johnson R P 2018 Review of medical radiography and tomography with proton beams *Rep. Prog. Phys.* 81 016701
[23] Chen G, Singh R, Castro J, Lyman J and Quivey J 1979 Treatment planning for heavy ion radiotherapy *J. Radiat. Oncol. Biol. Phys.* 5 1809–19
[24] Alpen E, Saunders D, Chatterjee A, Llacer J, Chen G and Scherer J 1985 A comparison of water equivalent thickness measurements: CT method versus heavy ion beam technique *Br. J. Radiol.* 58 542–8
[25] Paganetti H, 2012 Range uncertainties in proton therapy and the role of Monte Carlo simulations, Phys. Med. Biol. 57, R99–R117.
[26] Schneider U, Pedroni E, and Lomax A, 1996 The calibration of CT Hounsfield units for radiotherapy treatment planning, Phys. Med. Biol. 41, 111–124.
[27] Rietzel E, Schardt D, and Haberer T, 2007 Range accuracy in carbon ion treatment planning based on CT-calibration with real tissue samples, Radiat. Oncol. 2:14.
[28] Johnson R P *et al* 2016 A fast experimental scanner for proton CT: technical performance and first experience with phantom scans *IEEE Trans. Nucl. Sci.* 63 52
[29] Bucciantonio M, Amaldi U, Sauli F and Watts D 2013 Development of a fast proton range radiography system for quality assurance in hadrontherapy *Nucl. Instrum. Methods* A 732 564–7
[30] Naimuddin M *et al* 2016 Development of a proton computed tomography detector system *J. Instrum.* 11 C02012 [31] Scaringella M *et al* 2013 The PRIMA (PRoton IMAging) collaboration: development of a proton computed tomography apparatus *Nucl. Instrum. Methods* A 730 178–83
[32] Saraya Y, Izumikawa T, Goto J, Kawasaki T and Kimura T 2014 Study of spatial resolution of proton computed tomography using a silicon strip detector *Nucl. Instrum. Methods* A 735 485–9
[33] Taylor J T *et al* 2015 Proton tracking for medical imaging and dosimetry *J. Instrum.* 10 C02015

[34] Pemler P, Besserer J, de Boer J, Dellert M, Gahn C, Moosburger M, Schneider U, Pedroni F and Stäuble H 1999 A detector system for proton radiography on the gantry of the paul-scherrer-institute *Nucl. Instrum. Methods Phys. Res.* A 432 483–95
[35] Lo Presti D *et al* 2016 Design and characterization of a real time proton and carbon ion radiography system based on scintillating optical fibres *Phys. Med.* 32 1124–34
[36] Schulte R, Penfold S, Tafas J and Schubert K 2008 A maximum likelihood proton path formalism for application in proton computed tomography *Med. Phys.* 35 4849–56
[37]Plautz T *et al* 2014 200 MeV proton radiography studies with a hand phantom using a prototype proton CT scanner *IEEE Trans. Med. Imaging* 33 875–81
[38] Plautz T E *et al* 2016 An evaluation of spatial resolution of a prototype proton CT scanner *Med. Phys.* 43 6291
[39] Tillman I, Dettmann M, Herrig V, Thune Z, Zieser A, Michalek S, Been M, Martinez-Szewczyk M, Koster H, Wilkinson C, Kielty M, Jacobsohn L, Akgun U, 2017 High-Density Scintillating Glasses for A Proton Imaging Detector, Journal of Optical Materials, 68, 58-62.
[40] Agostinelli S. *et al.* 2003 Geant4 – A Simulation Toolkit, Nucl. Instr. and Meth. A, 506, 250-303
[41] Allison J. *et al.*, 2006 Geant4 Developments and Applications, IEEE Trans. on Nucl. Sci., 53, 1 270-278
[42] Wilkinson C, Ruane L, Miller W, Gunsch A, Zieser A, Tillman I, Thune Z, Wang D, Akgun U, 2018, CARNA – A Compact Glass Proton Imager, Proceedings of IEEE Nuclear Science Symposium and Medical Imaging Conference, DOI: 10.1109/NSSMIC.2017.8533076.
[43] Wilkinson C, Goranson K, Turney A, Xie Q, Tillman I, Thune Z, Dong A, Pritchett D, McInally W, Potter A, Wang D, Akgun U, 2017, High density scintillating glass proton imaging detector, Proc. SPIE 10132, Medical Imaging 2017: Physics of Medical Imaging, 101323V; doi:10.1117/12.2252777
[44] Varney G, Dema C, Gul B E, Wilkinson C, Akgun U, 2019, Use of Machine Learning in CARNA Proton Imager, Proc. SPIE 10948, Medical Imaging 2019: Physics of Medical Imaging, 109485P (1 March 2019); doi: 10.1117/12.2512565.
[45] Rescigno R, Bopp C, Rousseau M, Brasse D, 2015 A Pencil Beam Approach to Proton Computed Tomography, Med. Phys. 42 (11), 6610-6624
[46] Jan S, Santin G, Strul D, et al. GATE: a simulation toolkit for PET and SPECT. Phys Med Biol. 2004;49(19):4543-4561. doi:10.1088/0031-9155/49/19/007
[47] Jan S, Benoit D, Becheva E, et al. 2011, GATE V6: a major enhancement of the GATE simulation platform enabling modelling of CT and radiotherapy. Phys Med Biol.;56(4):881-901. doi:10.1088/0031-9155/56/4/001
[48] Sarrut D, Bardiès M, Boussion N, et al. 2014, A review of the use and potential of the GATE Monte Carlo simulation code for radiation therapy and dosimetry applications. Med Phys.;41(6): 064301 doi:10.1118/1.4871617
[49] https://doi.org/10.7937/K9/TCIA.2016.ACWOGBEF
[50] https://doi.org/10.7937/K9/TCIA.2016.QHSYHJKY
[51] https://doi.org/10.7937/K9/TCIA.2016.SQ4M8YP4
[52] https://doi.org/10.7937/K9/TCIA.2017.8oje5q00
[53] https://doi.org/10.7937/K9/TCIA.2016.LXKQ47MS
[54] https://imagej.nih.gov/ij/